

# Single-shot ptychography at a soft X-ray free-electron laser

Konstantin Kharitonov (✉ [konstantin.kharitonov@desy.de](mailto:konstantin.kharitonov@desy.de))

Deutsches Elektronen-Synchrotron DESY

Masoud Mehrjoo

Deutsches Elektronen-Synchrotron DESY

Mabel Ruiz-Lopez

Deutsches Elektronen-Synchrotron DESY

Barbara Keitel

Deutsches Elektronen-Synchrotron DESY

Svea Kreis

Deutsches Elektronen-Synchrotron DESY

Seung-gi Gang

Deutsches Elektronen-Synchrotron DESY

Rui Pan

Deutsches Elektronen-Synchrotron DESY

Alessandro Marras

Deutsches Elektronen-Synchrotron DESY

Jonathan Correa

Deutsches Elektronen-Synchrotron DESY

Cornelia Wunderer

Deutsches Elektronen-Synchrotron DESY

Elke Plonjes

Deutsches Elektronen-Synchrotron DESY

---

## Article

### Keywords:

**Posted Date:** May 13th, 2022

**DOI:** <https://doi.org/10.21203/rs.3.rs-1629463/v1>

**License:**   This work is licensed under a Creative Commons Attribution 4.0 International License.

[Read Full License](#)

---



# Single-shot ptychography at a soft X-ray free-electron laser

Konstantin Kharitonov<sup>1,\*</sup>, Masoud Mehrjoo<sup>1</sup>, Mabel Ruiz-Lopez<sup>1</sup>, Barbara Keitel<sup>1</sup>, Svea Kreis<sup>1</sup>, Seung-gi Gang<sup>1</sup>, Rui Pan<sup>1</sup>, Alessandro Marras<sup>1,2</sup>, Jonathan Correa<sup>1,2</sup>, Cornelia Wunderer<sup>1,2</sup>, and Elke Plönjes<sup>1</sup>

<sup>1</sup>Deutsches Elektronen-Synchrotron DESY, Germany

<sup>2</sup>Center for Free-Electron Laser Science CFEL, Deutsches Elektronen-Synchrotron DESY, Germany

\*konstantin.kharitonov@desy.de

## ABSTRACT

Ptychography is a scanning coherent diffraction imaging technique capable of providing images of extended samples with diffraction-limited resolution. However, ptychography experiments are time-consuming due to their scanning nature which also prevents their use for imaging of dynamical processes. Recently, setups based on two con-focal lenses were proposed to perform single-shot ptychography in the visible regime by measuring the diffraction pattern produced by multiple overlapping beams in one shot. However, this approach cannot be extended straightforwardly to X-ray wavelengths due to the application of refractive optics. In this work, we demonstrate a novel and nascent single-shot ptychography setup utilizing the combination of X-ray focusing optics with a two-dimensional beam-splitting diffraction grating. It allows single-shot imaging of extended samples at X-ray wavelengths. As a proof of concept, we performed single-shot ptychography in the XUV range at the free-electron laser FLASH and obtained a high-resolution reconstruction of the sample.

## Introduction

Ptychography is a scanning coherent diffraction imaging (CDI) technique capable of high-resolution imaging of extended objects<sup>1</sup>. Compared to the other scanning imaging techniques such as atomic force microscopy and scanning electron microscopy, ptychography is less damaging for the sample and can measure thick samples. Ptychography is based on the measurement of multiple diffraction patterns during scanning a photon beam over a sample. The acquired patterns are utilized in a phase retrieval procedure to reconstruct the complex beam (hereafter called probe) wavefield and, at the same time, the object transmission function. Scanning is performed so that it achieves a controlled degree of overlap between adjacent scan points. The overlap ensures the convergence stability of the reconstruction, prevents reconstruction ambiguities, and enables a simultaneous reconstruction of both probe and sample.

Recently, classical ptychography was successfully implemented at X-ray free-electron laser (FEL) light sources for both, imaging applications and photon beam characterization<sup>2-4</sup>. The ultra-high brightness and spatial coherence of the FEL radiation significantly decrease the data acquisition time for both, full-field and scanning imaging techniques. The femtosecond length of the FEL pulses can enable imaging of dynamical processes with unprecedented temporal resolution. However, ptychography in its conventional scanning mode cannot capture dynamics of systems. Therefore, implementation of single-shot ptychography using X-rays can greatly enhance the potential of imaging at FEL sources and enable diffraction-limited time-resolved imaging of extended samples and dynamics of complex matters at X-ray regimes.

Single-shot ptychography was first proposed by Sidorenko et al.<sup>5</sup> and was further expanded to Fourier<sup>6</sup>, multi-slice<sup>7</sup> and multi-wavelength<sup>8</sup> regimes in the visible range. A setup based on a 4-f lens arrangement is capable of performing simultaneous illumination of a sample by the multiple beamlets in one shot by utilizing a pinhole array placed in the front focal plane of the first lens as a light source. The sample is placed close to the common focal plane of the two lenses. The overlap of the beamlets produced by the individual pinholes can be adapted by adjusting the focus-sample distance. However, this concept cannot be directly transferred to the X-ray regime due to the lack of efficient high numerical aperture refractive optics at these wavelengths.

As an alternative, we propose a setup based on combining bendable Kirkpatrick-Baez (KB) optics for the XUV and soft X-ray range with a beam-splitting two-dimensional (2D) diffraction grating inspired by the work of Pan et al.<sup>9</sup>. The schematic diagram of the proposed setup is shown in Fig.1. This setup allows illuminating the sample by multiple beamlets in one shot by placing it in the vicinity of the beam-splitting diffraction grating. The grating splits the incoming FEL beam into a number of beamlets (shown in red, green, and blue in Fig.1). The degree of overlap of the beamlets and the field of view (FOV) (i.e. the

total area of illumination on the sample) is determined by the specific design of the grating. Moreover, it is possible to optimize both: the degree of overlap of the beamlets on the sample and the FOV. The former is adjusted by changing the grating-sample distance, while the latter is adapted by varying the focal length of the bendable KB mirrors<sup>10,11</sup>.

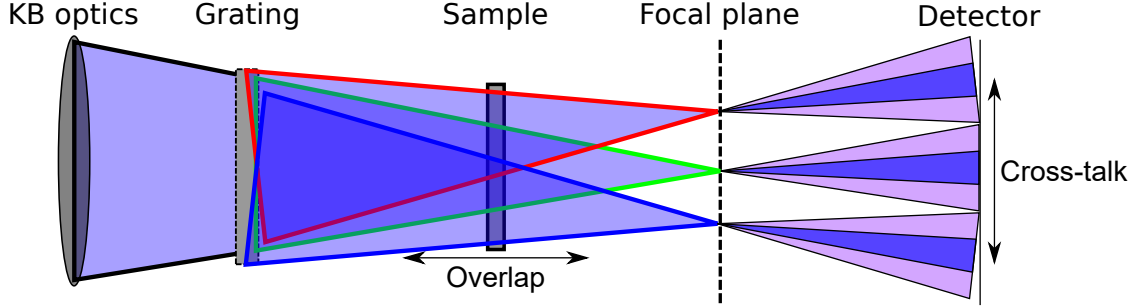


**Figure 1.** A schematic 2D diagram of the proposed experimental setup. The FEL beam is focused downstream of the sample by the KB mirrors. The beam-splitting grating is placed in front of the sample and splits the beam into several diffraction orders (shown in red, green, and blue). The sample, placed in the vicinity of the grating, is illuminated by the overlapping beamlets produced by the grating. The degree of overlap and the field of view in the sample plane can be controlled by changing the grating-sample distance. The detector is placed downstream of the focal plane. The focal length of the KB mirrors is selected to facilitate the separation of the beamlets (dark blue) and minimize the possible cross-talk between the radiation scattered by the sample (light-purple).

For the reconstructions we used an automatic differentiation<sup>12</sup> (AD) powered Ptychography engine described in our previous work<sup>2</sup>. AD is capable of numerically obtaining the gradients of any differentiable function with respect to its arguments. This allows splitting the Ptychography reconstruction into three independent parts: a forward model describing the intensity formation at the detector plane and allowing the approximation of the measured intensity, a loss function qualitatively evaluating the difference between the measured and approximated intensities, and a gradient-based optimizer which utilizes the gradients of the loss function to minimize it and find the appropriate values for sample, probe, and other reconstructable parameters.

Here, we report on an X-ray compatible setup developed for performing single-shot Ptychography at FELs. As an experimental proof of concept, the single-shot Ptychographic technique was demonstrated at the FLASH2<sup>13</sup> variable micro-focus beamline FL24<sup>10</sup>.

## Methods

### Ptychography formalism

In classical Ptychography, a sample  $O$  is scanned by a probe  $P$  in numerous positions characterized by the displacement vectors  $\mathbf{r}_j, j \in 1..N$  where  $N$  is the number of scan points. Under the thin sample approximation<sup>14</sup>, the exit wave  $\Psi_j$  produced at the  $j$ -th position may be expressed as  $\Psi_j = P \cdot O_{\mathbf{r}_j}$ . The intensity produced by the exit-wave at the detector may be calculated as:

$$I_j = |\mathcal{P}\{\Psi_j\}|^2, \quad (1)$$

where  $\mathcal{P}$  is the propagator defined by the geometry of the experiment and the Fresnel number<sup>15</sup>. The Fresnel number is given as  $\frac{a^2}{\lambda z}$ , where  $a$  is the characteristic size of the illuminated area,  $z$  is the propagation distance and  $\lambda$  is the wavelength of the radiation. During the Ptychography reconstruction, the multiple intensity patterns are used to perform phasing and to reconstruct the complex-valued  $P$  and  $O$  functions.

This task can be viewed as an optimisation task of finding a pair of  $P$  and  $O$  that minimizes a loss function  $\mathcal{E}(I_j, \tilde{I}_j)$  evaluating the similarity between  $I_j$  (measured) and  $\tilde{I}_j$  (estimated) intensity at the  $j$ -th scan position. The minimization can be performed by gradient-based optimization methods<sup>16</sup> utilizing automatic differentiation. AD is capable of dynamically estimating gradients of any differentiable function with respect to its parameters. This makes a Ptychographic reconstruction feasible when an appropriate differentiable forward model describing the particular experiment is provided<sup>2,17</sup>. The additional important components of the AD-powered Ptychography reconstruction are a loss function and a gradient-based optimizer. A loss function evaluates the quality of reconstruction by comparing the approximated and measured intensity distributions. Additionally, various regularization terms can be included in the loss function to perform the denoising and speed up the convergence. In this work, the loss function is used in the following form:

$$L(I, \tilde{I}, O) = \mathcal{E}(I, \tilde{I}) + TVD(O) = \frac{1}{N_d} \sum_m \|\sqrt{I_m} - \sqrt{\tilde{I}_m}\|^2 + \gamma \sum_{i,k}^{N-1} \sqrt{|O_{i+1,k} - O_{i,k}|^2 + |O_{i,k+1} - O_{i,k}|^2} \quad (2)$$

57 where  $\tilde{I}$  is the approximation of the intensity provided by the forward model,  $I$  is the measured intensity,  $N_d$  is the total number  
 58 of pixels of the used 2D detector,  $N$  is the number of pixels in a specific row or column,  $\gamma$  is the regularization weight which  
 59 should be selected individually to ensure the stability of the reconstruction, and  $TVD$  stands for the total variation denoising  
 60 regularizer<sup>18</sup>.

Although initially ptychography was developed under the assumption of a fully-coherent and spatially stable beam, the  
 actual X-ray probe beam may not fully meet these requirements and necessitate a modification of the forward model. Potentially,  
 an only partial spatial coherence of the probe must be taken into account as proposed by Thibault et al.<sup>19</sup>. In this case, the  
 probe can be expressed as a set of mutually incoherent orthogonal modes  $M_i$  which allows describing the measured intensity as  
 follows:

$$I_j = \sum_i |\mathcal{P}\{O \cdot M_i\}|^2. \quad (3)$$

Furthermore, the probe positions in the sample plane  $r_j$  can be determined only with some experimental uncertainty and may  
 need to be treated as optimizable variables during the reconstruction process. We utilized the differentiable affine transformer<sup>2</sup>  
 to calculate the transfer function of the sample at the positions of the different beamlets. In this formalism a shifted sample  
 transfer function can be represented as follows:

$$O_{\mathbf{r}_j} = \mathcal{A}_{\theta_j}(O), \quad (4)$$

61 where  $\mathcal{A}_{\theta_j}$  represents the affine transform operator  $\mathcal{A}$  driven by its parameter matrix  $\theta$ . This operator is differentiable with  
 62 respect to both coordinates, position  $\mathbf{r}_j$  and object function  $O$ . Thus, the set of the correct probe positions  $\mathbf{r}_j$  can be found  
 63 through the gradient-based optimization of  $\theta_j$ .

#### 64 Single-shot ptychography

Single-shot ptychography further develops classical ptychography by recording the entire set of diffracted intensities simulta-  
 neously utilizing a single FEL pulse rather than scanning different sample positions consecutively. This can be realized by  
 splitting the probe  $P$  into several beamlets  $B_j$ , that mutually overlap on the sample surface, using a 2D diffraction grating.  
 For successful phase retrieval in single-shot ptychography, two key prerequisites need to be met for the measured intensity  
 distribution. First, a functional dependence has to exist between the probe and the beamlets:  $B_j = g_j(P)$ , which links the initial  
 probe  $P$  with the  $j$ -th beamlet  $B_j$ . In our case, using a 2D grating and fulfilling the conditions for a paraxial approximation, all  
 beamlets can be viewed as the original probe scaled with different intensity coefficients  $\alpha_j$  corresponding to the diffraction  
 efficiency of the grating  $B_j = g_j \cdot P$ . Due to this dependency, the forward model can be expressed directly with respect to the  
 probe  $P$ . Thus, there is no need for optimization of each of the beamlets  $B_j$ , which greatly reduces the number of optimizable  
 variables and ensures convergence. As a second prerequisite, the diffracted intensity of each of the out-waves of the beamlets  
 should ideally be localized and separable from its neighbors without cross-talk. Thus, each localized intensity  $I_j \in I$  can be  
 attributed to a unique beamlet. When both conditions are fulfilled, the measured intensity can be numerically formulated as  
 follows:

$$I_{meas} = \sum_j^N I_j = \sum_j^N |\mathcal{P}\{B_j \cdot O_{\mathbf{r}_j}\}|^2 = \sum_j^N |\mathcal{P}\{g_j(P) \cdot O_{\mathbf{r}_j}\}|^2. \quad (5)$$

65 Both key criteria are held in our proposed scheme as follows: an FEL probe is focused by the KB mirrors downstream  
 66 of the sample. The probe is split by a 2D diffraction grating placed in the vicinity of the sample. The combination of the  
 67 grating-detector distance and focal distance of the KB is set to obtain an overlap of  $\sim 80\%$  at the sample plane. The grating  
 68 parameters are chosen appropriately to match the produced diffraction pattern to the detector chip and pixel sizes. The resolution  
 69 of the reconstruction is limited by the highest scattering angle registered for a particular beamlet. When the illumination is  
 70 arranged in a  $x \times x$  square, the maximum achievable resolution can be estimated as  $\frac{\lambda z x}{Np}$ , where  $\lambda$  is the wavelength,  $z$  is the  
 71 sample-detector distance,  $N$  is the number of pixels of the detector, and  $p$  is the detector pixel size<sup>14</sup>. The number of measurable  
 72 localized diffraction patterns is set by the specification of the beam-splitting grating and detector parameters which defines the  
 73 trade-off between the FOV, the maximum achievable resolution, and the ptychographic oversampling requirement.<sup>20,21</sup>

74 The design of the beam-splitting grating should facilitate a clear separation of the beamlet diffraction patterns at the detector  
 75 plane, which minimizes the cross-talk and leads to maximum spatial resolution in the reconstruction. Additionally, the resulting  
 76 diffraction efficiency of the grating orders should be set as evenly as possible to reduce the required dynamical range of the  
 77 detector. Further details on the grating parameters can be found in the [Experimental setup](#) section. Such optimization of the  
 78 grating allowed us to simultaneously measure diffraction from (0, 0) up to (2, 3) grating order depending on the detector chip  
 79 size. Thus, at a given wavelength, the angular size of the detector chip is the main factor limiting the number of recorded  
 80 beamlets and the resulting FOV of the reconstruction.

## 81 Single-shot forward model

Our forward model for single-shot ptychography approximates the intensity  $I_j$  produced by  $j$ -th beamlet  $B_j$  as follows:

$$I_j = \alpha_j \sum_i \left| \mathcal{P}_2 \left\{ \mathcal{A}_{\theta_j}(O) \cdot \mathcal{P}_1 \{M_i \cdot S\} \right\} \right|^2, \quad (6)$$

where  $\mathcal{P}_1$  is the Fresnel transfer function propagator in the near field<sup>22</sup> describing the propagation of the probe from the grating plane to the object plane,  $\mathcal{P}_2$  is the Fresnel propagator in the intermediate field<sup>22</sup> describing the propagation of the out-wave from the sample plane to the detector plane,  $S$  is the support representing the active area of the grating,  $\mathcal{A}_{\theta_j}$  represents an affine transform and  $\alpha_j$  is the scaling coefficient representing grating efficiency for  $j$ -th diffraction order.  $\mathcal{P}_1$  and  $\mathcal{P}_2$  are implemented as follows:

$$\mathcal{P}_1(\Psi_{\rho_0}) = \mathcal{F}^{-1} \left\{ \mathcal{F} \{ \Psi_{\rho} \} \cdot e^{(jkz)} \exp(-j\pi\lambda z(q_x^2 + q_y^2)) \right\} \quad (7)$$

$$\mathcal{P}_2(\Psi_{\rho_0}) = \Psi_{\rho_1} = -\frac{i}{\lambda z} \exp(i\frac{k}{2z}\rho_1^2) \cdot \mathcal{F} \left\{ \exp(i\frac{k}{2f}\rho_0^2) \Psi_{\rho_0} \right\}, \quad (8)$$

82 where  $\Psi_{\rho}$  is the complex wavefield,  $z$  is the propagation distance,  $k$  is the wave number,  $\rho = (x, y)$ ,  $\rho_0$  and  $\rho_1$  denote the  
83 transverse coordinates at the initial and resulting plane respectively,  $\mathcal{F}$  and  $\mathcal{F}^{-1}$  denote the forward and inverse Fourier  
84 transform while  $q_x, q_y$  are the coordinates in the Fourier space.

85 Thus, during the reconstruction the following parameters are optimized: object function  $O$ , probe modes  $M_i$ , scan coordinates  
86  $r_j$  expressed through the affine parameters  $\theta_j$ , grating-sample distance  $z_{gs}$  included into the ASM propagator  $\mathcal{P}_1$ , and order-  
87 specific diffraction grating efficiency  $\alpha_j$ . The optimization was performed using the ADAM<sup>16</sup> optimizer. The algorithm of the  
88 AD-powered ptychographic reconstruction is illustrated below.

---

### Algorithm 1: AD-powered ptychographic reconstruction

---

**Data:** Measured intensities  $I_j$ , scan positions  $r_j$ , initial guesses of the probe  $P$ , object  $O$ , grating-sample distance  $z_{gs}$ ,  
grating efficiencies  $\alpha_j$ , learning rates  $lr$  for each optimizable parameter, regularization weight  $\gamma$ , number of  
iterations  $N$ .

**for**  $n \in 0 \dots N$  **do** // Global iterations

**for**  $j \in J$  **do** // iterations through scan positions

        // Calculate intensity with the forward model

$$I_j \leftarrow \alpha_j \sum_i \left| \mathcal{P}_2 \left\{ \mathcal{A}_{\theta_j}(O) \cdot \mathcal{P}_1 \{M_i \cdot S\} \right\} \right|^2$$

        /\* Calculate loss function  $L(I, \tilde{I}, O)$  as a sum of the  $\mathcal{E}(I, \tilde{I})$  - error between the  
        approximated and measured intensities and  $TVD(O)$  - regularization term \*/

$$L(I, \tilde{I}, O) \leftarrow \frac{1}{N_d} \sum_m^N \|\sqrt{I_m} - \sqrt{\tilde{I}_m}\|^2 + \gamma \sum_{i,k}^{N-1} \sqrt{|O_{i+1,k} - O_{i,k}|^2 + |O_{i,k+1} - O_{i,k}|^2};$$

        Calculate gradients of the  $L$  w.r.t. all optimizable parameters

        Update all of the parameters by performing a step of the ADAM optimization

**Result:** Reconstructed object  $O$ , probe  $P$ , refined scan positions  $r_j$ , grating-sample distance  $z_{gs}$ , grating efficiencies  $\alpha_j$

---

## 90 Experiment and results

### 91 Experimental setup

92 As a proof of principle, the proposed concept for single-shot ptychography was realized at the soft X-ray FEL FLASH. The  
93 experiment was performed at the FLASH2 beamline FL24 using a wavelength  $\lambda = 13.5 \text{ nm}$  i.e. a photon energy  $E_{ph} = 91.8 \text{ eV}$ .  
94 The experimental setup is shown in Fig.2. Metal foil filters in combination with a gas attenuator<sup>10,23</sup> were used to attenuate  
95 the fundamental photon beam energy to appropriate levels and to suppress higher FEL harmonics. The FEL beam was  
96 focused using a pair of bendable KB mirrors<sup>24</sup> to a focal spot position of  $9 \text{ cm}$  behind the sample<sup>10,11</sup>. A 2D beam-splitting  
97 transmission-grating with a period  $L = 2.930 \mu\text{m}$ , an opening size  $G = 0.732 \mu\text{m}$  and an active area of  $200 \times 200 \mu\text{m}^2$  was  
98 placed  $210 \text{ cm}$  after the center of the last KB mirror. The grating was made from a  $200 \text{ nm}$  thick gold layer electroplated on a  
99  $50 \text{ nm}$  silicon nitride membrane. The active area of the grating was smaller ( $\sim 1/4$ ) than the beam cross-section at the grating

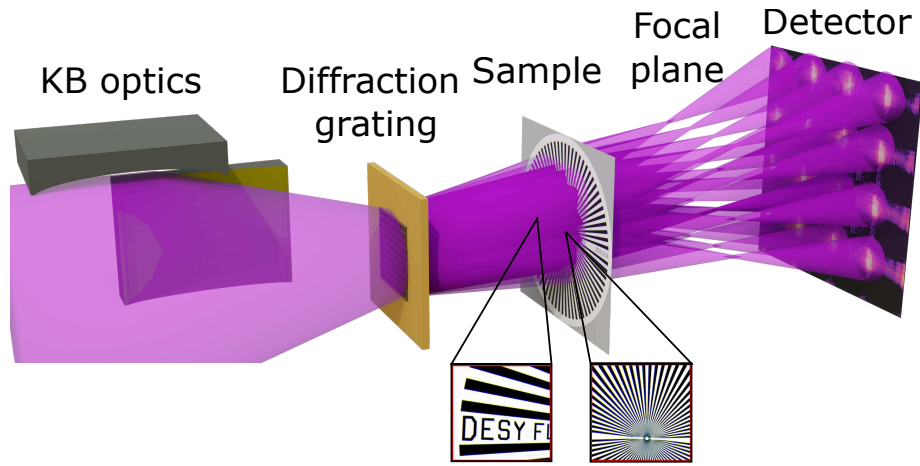


**Figure 2.** Schematic of the experimental setup. The FEL beam was focused 9 cm after the sample using bendable KB mirrors. The beam-splitting 2D diffraction grating was placed 210 cm after the center of the last KB mirror. The sample was placed approximately 0.9 cm behind the grating and thus illuminated by the overlapping beamlets produced by the grating. The two areas of the sample 'letters' and 'stripes' are shown in the insets. The ANDOR iKon-M SO CCD was placed in the intermediate field 66 cm downstream of the sample. Alternatively, the PERCIVAL detector was placed in the intermediate field 135 cm downstream of the sample.

100 plane to select the most intense part of it and increase the spatial coherence. The sample was placed 0.9 cm downstream of the  
 101 grating, which led to an average mutual overlap of 80% between neighboring beamlets in the sample plane. The diffraction  
 102 patterns were measured using two detectors: an ANDOR iKON-M SO CCD camera ( $1024 \times 1024$  pixels,  $13 \times 13 \mu\text{m}^2$  each)  
 103 and the novel PERCIVAL detector ( $1440 \times 1484$  pixels,  $27 \times 27 \mu\text{m}^2$  each)<sup>25</sup>. The PERCIVAL detector offers an exceptionally  
 104 high dynamical range ( $5 \times 10^4$  photons at  $E_{ph} = 100\text{eV}$ ) and large chip size ( $3.8 \times 4\text{cm}^2$ ). The sample-to-detector distances  
 105 were selected to fit at least  $4 \times 4$  beamlets onto the detector chip. It was 66 cm for the ANDOR camera and 135 cm for the  
 106 PERCIVAL detector, respectively.

### 107 Data treatment and reconstruction

108 In single-shot ptychography, measured intensities must be properly tessellated and then segmented into separate diffraction  
 109 patterns each attributed to a single beamlet. The patterns later are placed in equal-sized computational frames used for the  
 110 numerical light propagation. A possible angle between the grating and detector axes, which is experimentally difficult to avoid,  
 111 prevents the use of any tessellation strategy based on the grating-detector geometry. To perform the data processing, we adopted  
 112 a segmentation routine proposed by Barolak et al.<sup>8</sup> which is based on Voronoi tessellation. This algorithm finds so-called  
 113 Voronoi cells  $v_j$  for a given set of the points  $p_j$ , where each cell is defined as a set of detector pixels that are closer to one  
 114 particular point than to any other. The process of data segmentation is illustrated in Fig.3. The orientation of the grating axes  
 115 with respect to the detector pixels axes can be found by utilizing the centers of mass of the intensity patterns produced by the  
 116 individual diffraction orders (shown by the green dots in Fig.3). The horizontally and vertically diffracted orders ( $(0, x)$  and  
 117  $(x, 0)$  diffraction orders) form a basis of the grating coordinate system and thus can be used to calculate the coordinates of all the  
 118 diffraction orders at the detector plane. These coordinates were used as the input points  $p_j$  for the Voronoi tessellation resulting  
 119 in the Voronoi cells shown with the red polygons. Each of these cells surrounds a part of the detector in which all the intensity  
 120 must be attributed to a particular diffraction order. The scan coordinates at the sample plane  $r_j$  corresponding to each order  
 121 were estimated from the diffraction grating parameters and the grating-sample distance. In turn, the size of the computational  
 122 frames for the light propagation was found as the smallest square simultaneously circumscribed about and concentric with the  
 123 largest Voronoi cell (shown with green squares in Fig.3). Since in some of the frames only part of the pixels (fitting inside the  
 124 particular Voronoi cell shown with the red polygons in Fig.3) could be reliably attributed to the corresponding diffraction order,  
 125 the area outside the Voronoi cells (red polygons) was left unconstrained during the reconstruction.

126 The segmented data was used as the input for the single-shot ptychography reconstruction performed using an AD-based  
 127 forward model. Diffraction patterns of the grating measured without the sample in place were used to initialize the probe  
 128 modes  $M_i$  and grating efficiencies  $\alpha_j$ . The approximate complex wavefields of all the diffraction orders at the detector plane  
 129 were calculated utilizing the known defocus produced by the KB. The back-propagated wavefields were orthogonalized using  
 130 a singular value decomposition and used as the initial values for the  $M_j$ . The diffraction efficiencies of the grating  $a_j$  were  
 131 estimated as the ratio of the intensity of the  $(0, 0)$  order to the intensities diffracted to the other orders. At the same time, the

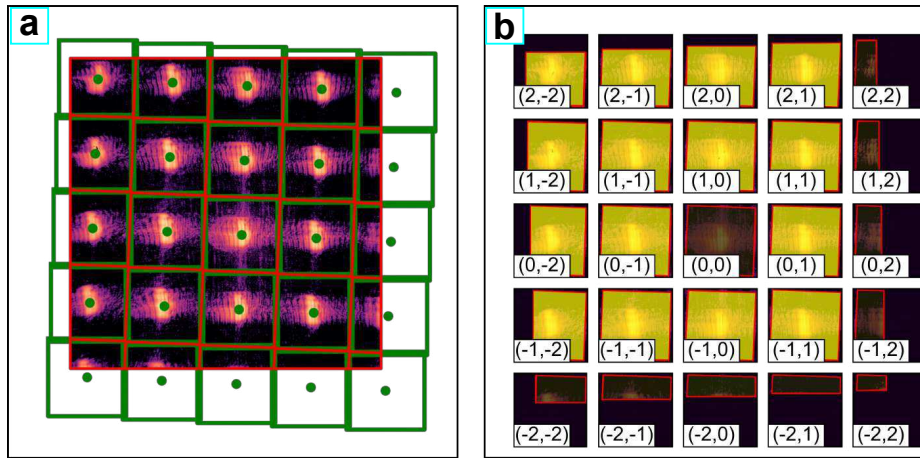


**Figure 3.** Illustration of the segmentation of the diffraction pattern. **(a)** Voronoi tessellation of the measured data. Centers of masses of sub-patterns corresponding to each of the grating orders are shown with green dots. Red polygons represent individual Voronoi cells fitting in the area of the detector chip. Green squares show the smallest square simultaneously circumscribed about and concentric with the largest Voronoi cell. **(b)** Split data used for the reconstruction. The area highlighted in yellow is inside the corresponding Voronoi cell and is constrained during the reconstruction. Each individual square is equivalent to a measurement from an individual beamlet and represents the individual computational frame used for the propagation of the respective diffraction order. The coordinates of the individual diffraction order at the sample plane can be estimated using the grating-sample distance and grating parameters. All the data pieces with the less than half of the pixels measured were ignored during the reconstruction (right- and lower- most squares, dark in (b)). The (0, 0) order was also ignored during the reconstruction due to high levels of parasitic scattering from the beam passing through the frame of the grating.

132 initial coordinates of the beamlets at the sample plane  $r_j$  were estimated from the known grating parameters and grating-sample  
 133 distance  $z_{gs}$ .

134 The reconstruction took  $6 \times 10^3$  iterations of the gradient-based optimization utilizing the ADAM optimizer. We utilized  
 135 NVIDIA Tesla P100 GPU for the computations, which resulted in an iteration time of 20 ms with a total reconstruction time of  
 136 2 min. The regularization weight  $\gamma$  and respective learning rates for the optimizable parameters were selected to provide fast  
 137 and stable convergence.

138 The raw data with the averaged dark background subtracted are shown in Fig.4. Fig.4 **(a)** corresponds to the full  
 139 image measured by the Andor detector, while Fig.4 **(b)** corresponds to the central part of the image measured with the  
 140 PERCIVAL detector. The intensities produced by the different beamlets are separated with limited degree of cross-talk present.  
 141 Reconstructed samples and main probe modes are shown in Fig.4. The data leading to the reconstruction of the 'stripes' (Fig.4  
 142 (c, e)) and 'letters' (Fig.4 (d, f)) areas were measured using the Andor and PERCIVAL detectors, respectively. The FLASH  
 143 beam was apertured by the grating frame but nevertheless, to refrain from raising any source of uncertainty we have applied  
 144 the multimodal approach. The occupancies of the main reconstructed modes are shown in Fig.4(c,d) lower left corners. As  
 145 expected, the results were not drastically changed using the partially coherent approximation.

146 The resolution of the reconstructions was evaluated using Fourier ring correlation<sup>26</sup>. The resolution at the 0.5 bit cut-off  
 147 was found to be approximately  $4.9 \mu\text{m}$  and  $5.6 \mu\text{m}$  for 'stripes' and 'letters' regions respectively (red dashed lines in Fig. 5  
 148 (a),5 (b)). The lower resolution of the 'letters' area reconstruction can be explained by discontinuities in the probe wavefield  
 149 (Fig. 4(f)) resulting from the shape of the SASE pulses during the measurement of the 'letters' area.

## 150 Discussion

151 Splitting of the measured diffraction pattern was performed utilizing Voronoi tessellation. This method does not require any a  
 152 priori assumptions about grating-detector orientation and allows an automatic data treatment. Moreover, in the general case,  
 153 this method gives the most optimal partition since any derivation from the Voronoi cells will result either in increasing the  
 154 cross-talk or in reducing the maximum achievable resolution due to decreasing of the maximum registered angle of diffraction  
 155 from the sample.

156 The reconstruction was initiated using an unknown probe wavefield and grating transfer function. The initial probe guess  
 157 was obtained from the averaged intensity measured without the sample and back-propagated to the sample plane. The grating

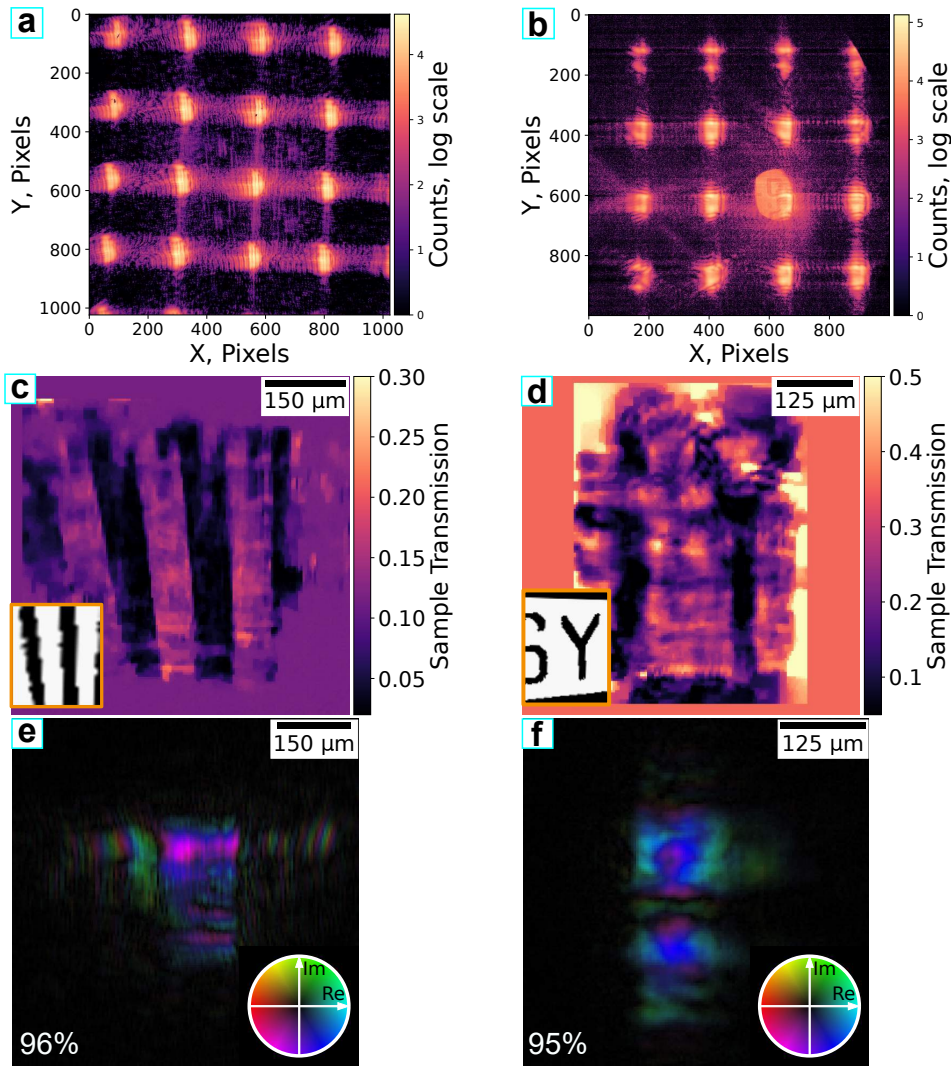


**Figure 4.** Raw data and results of the single-shot ptychography reconstructions. (a),(b) Raw data used for the reconstructions of the (c) - 'stripes' and (d) - 'letters' regions of the sample. (a) and (b) were measured using the Andor and the PERCIVAL detector respectively. (c),(d) Reconstructed sample transmission for (c) - 'stripes' and (d) - 'letters' regions of the Siemens star sample. (e),(f) Reconstructed complex wavefields of the main probe mode corresponding to (b) and (c) respectively. Percentages in the lower left corner represent the occupancy of the main mode.

158 transmission function was assumed to affect only the intensity of the particular beamlet under the paraxial approximation.  
 159 However, the quality of the reconstruction may be improved by performing a preliminary beam and grating characterization and  
 160 taking the non-paraxial effects<sup>27</sup> into account. This could be achieved by additional scanning ptychography measurements done  
 161 on the beam-splitting grating itself with the same setup. However, this would require placing the grating on a high-precision  
 162 motorized stage to scan the grating itself with nanometer resolution, as described in Kharitonov et al.<sup>2</sup>, thus increasing the  
 163 complexity of the experimental setup.

164 Imaging in the intermediate field geometry resulted in interference between neighboring beamlets and thus a cross-talk  
 165 when splitting the data for reconstruction. These effects can be avoided by placing the detector closer to the focal plane of  
 166 the KB, thus resulting in a lesser degree of cross-talk. However, this would require a much higher dynamical range of the  
 167 detector to measure the intensity distribution at higher scattering angles. Another possible approach could be to formulate an  
 168 alternative forward model capable of simulating the interference between neighboring beams. The overall diffraction pattern  
 169 can be expressed as the intensity of the coherent sum of separately propagated complex wavefields interfering at the detector  
 170 plane. This formalism can integrate the inter-beamlet interference fringes into the forward model and increase the resolution of  
 171 the reconstruction. However, this approach requires an optimization of the inter-beam phase difference, which might prevent the  
 172 convergence of the reconstruction. Overall, further development of the single-shot ptychography might increase the achievable

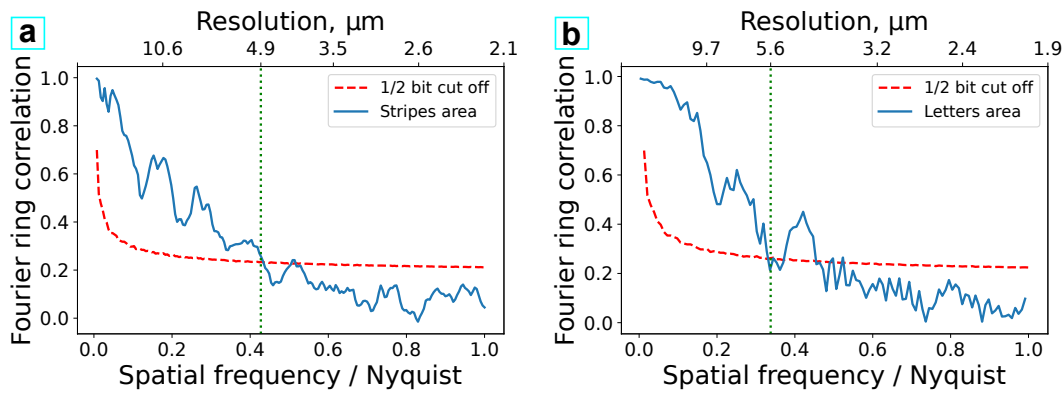


**Figure 5.** (a),(b) Estimated resolutions of reconstructions using Fourier ring correlation, (a),(b) correspond to Fig.4(c) and (d) respectively

173 resolution.

174 A 2D transmission grating was utilized to perform the splitting of the XUV beam. This resulted in a limited grating  
 175 efficiency and a high thermal load due to the absorbance of the radiation in the non-transparent areas. Use of a phase grating may  
 176 solve these problems, however, it may not be feasible for XUV wavelengths due to manufacturing restrictions. The mesh scan  
 177 pattern produced by the grating employed in our proof-of-principle experiment is highly symmetric and may cause raster-grid  
 178 pathology<sup>28</sup>. Design of a more elaborate fan-out<sup>29</sup> grating tailored for the particular setup and wavelength combination will  
 179 result in a more asymmetric scan pattern<sup>30</sup>. Additionally, it will improve the separation and minimize the cross-talk between  
 180 the neighboring beamlets in the detector plane. The use of a grating with a smaller period and higher angles of diffraction may  
 181 also simplify the intensity separation and improve the achievable resolution by increasing the maximal measured scattering  
 182 angle of the sample. This, however, would require reformulation of a forward model in a non-paraxial single-shot formalism<sup>27</sup>.

## 183 Conclusion

184 For the first time, single-shot ptychography was demonstrated at X-ray free-electron lasers. In a proof-of-principle experiment at  
 185 FLASH2, single-shot ptychography was experimentally adapted to the XUV and X-ray ranges. A differentiable forward model,  
 186 which allows analysis of highly fluctuating sources such as SASE type FELs<sup>31</sup>, was used for the AD-powered reconstruction of  
 187 the sample and probe functions without requiring preliminary knowledge of the grating transfer function or prior photon beam  
 188 characterization.

189 An improved experimental setup and an adaption of the computational model will extend the use of single-shot ptychography  
 190 at FELs to sliced 3D ptychography imaging of extended samples, allowing much higher sample throughput than scanning  
 191 methods. In combination with a pump-probe concept, the technique would allow to fully utilize the potential of the femtosecond-  
 192 long FEL pulses for ultra-fast time-resolved imaging of dynamical processes.

## 193 References

- 194 1. Guizar-Sicairos, M. & Thibault, P. Ptychography: A solution to the phase problem. *Phys. Today* **74**, 42–48 (2021).
- 195 2. Kharitonov, K. *et al.* Flexible ptychography platform to expand the potential of imaging at free electron lasers. *Opt. express*  
 196 **29**, 22345–22365 (2021).
- 197 3. Schropp, A. *et al.* Full spatial characterization of a nanofocused x-ray free-electron laser beam by ptychographic imaging.  
 198 *Sci. reports* **3**, 1–5 (2013).
- 199 4. Sala, S. *et al.* Pulse-to-pulse wavefront sensing at free-electron lasers using ptychography. *J. applied crystallography* **53**  
 200 (2020).
- 201 5. Sidorenko, P. & Cohen, O. Single-shot ptychography. *Optica* **3**, 9, DOI: [10.1364/OPTICA.3.000009](https://doi.org/10.1364/OPTICA.3.000009) (2016).
- 202 6. He, X., Liu, C. & Zhu, J. Single-shot fourier ptychography based on diffractive beam splitting. *Opt. Lett.* **43**, 214, DOI:  
 203 [10.1364/ol.43.000214](https://doi.org/10.1364/ol.43.000214) (2018).
- 204 7. Goldberger, D., Barolak, J., Durfee, C. G. & Adams, D. E. Three-dimensional single-shot ptychography. *Opt. Express* **28**,  
 205 18887–18898 (2020).

- 206 **8.** Barolak, J. *et al.* Wavelength-multiplexed single-shot ptychography. *Ultramicroscopy* **233**, 113418, DOI: [10.1016/j.](https://doi.org/10.1016/j.ultramic.2021.113418)  
207 [ultramic.2021.113418](https://doi.org/10.1016/j.ultramic.2021.113418) (2022). [2009.01337](https://arxiv.org/abs/2009.01337).
- 208 **9.** Pan, X., Liu, C. & Zhu, J. Single shot ptychographical iterative engine based on multi-beam illumination. *Appl. Phys. Lett.*  
209 **103**, DOI: [10.1063/1.4826273](https://doi.org/10.1063/1.4826273) (2013).
- 210 **10.** Plönjes, E., Faatz, B., Kuhlmann, M. & Treusch, R. Flash2: Operation, beamlines, and photon diagnostics. In *AIP*  
211 *Conference Proceedings*, vol. 1741, 020008 (AIP Publishing LLC, 2016).
- 212 **11.** Ruiz-Lopez, M. Status of flash2 (conference presentation). In *X-Ray Free-Electron Lasers: Advances in Source*  
213 *Development and Instrumentation V*, vol. 11038, 110380F (International Society for Optics and Photonics, 2019).
- 214 **12.** Margossian, C. C. A review of automatic differentiation and its efficient implementation. *Wiley interdisciplinary reviews:*  
215 *data mining knowledge discovery* **9**, e1305 (2019).
- 216 **13.** Faatz, B. *et al.* Simultaneous operation of two soft x-ray free-electron lasers driven by one linear accelerator. *New J.*  
217 *physics* **18**, 062002 (2016).
- 218 **14.** Paganin, D. *et al.* *Coherent X-ray optics*. 6 (Oxford University Press on Demand, 2006).
- 219 **15.** Born, M. & Wolf, E. *Principles of optics: electromagnetic theory of propagation, interference and diffraction of light*  
220 (Elsevier, 2013).
- 221 **16.** Kingma, D. P. & Ba, J. Adam: A Method for Stochastic Optimization. *3rd Int. Conf. on Learn. Represent. ICLR 2015 -*  
222 *Conf. Track Proc.* 1–15 (2014). [1412.6980](https://arxiv.org/abs/1412.6980).
- 223 **17.** Du, M. *et al.* Adorym: a multi-platform generic x-ray image reconstruction framework based on automatic differentiation.  
224 *Opt. Express* **29**, 10000–10035 (2021).
- 225 **18.** Chambolle, A. An algorithm for total variation minimization and applications. *J. Math. imaging vision* **20**, 89–97 (2004).
- 226 **19.** Thibault, P. & Menzel, A. Reconstructing state mixtures from diffraction measurements. *Nature* **494**, 68–71 (2013).
- 227 **20.** Edo, T. *et al.* Sampling in x-ray ptychography. *Phys. Rev. A* **87**, 053850 (2013).
- 228 **21.** da Silva, J. C. & Menzel, A. Elementary signals in ptychography. *Opt. express* **23**, 33812–33821 (2015).
- 229 **22.** Voelz, D. G. & Roggemann, M. C. Digital simulation of scalar optical diffraction: revisiting chirp function sampling  
230 criteria and consequences. *Appl. optics* **48**, 6132–6142 (2009).
- 231 **23.** Hahn, U. & Tiedtke, K. The gas attenuator of flash at desy. In *AIP Conference Proceedings*, vol. 879, 276–282 (American  
232 Institute of Physics, 2007).
- 233 **24.** Raimondi, L. *et al.* Status of the kb bendable optics at fermi@ elettra fel. In *Adaptive X-Ray Optics III*, vol. 9208, 920804  
234 (International Society for Optics and Photonics, 2014).
- 235 **25.** Marras, A. *et al.* Percival: A soft x-ray imager for synchrotron rings and free electron lasers. In *AIP Conference*  
236 *Proceedings*, vol. 2054, 060060 (AIP Publishing LLC, 2019).
- 237 **26.** Banterle, N., Bui, K. H., Lemke, E. A. & Beck, M. Fourier ring correlation as a resolution criterion for super-resolution  
238 microscopy. *J. Struct. Biol.* **183**, 363–367, DOI: [10.1016/j.jsb.2013.05.004](https://doi.org/10.1016/j.jsb.2013.05.004) (2013).
- 239 **27.** Chang, C. *et al.* 3d single-shot ptychography with highly tilted illuminations. *Opt. Express* **29**, 30878–30891 (2021).
- 240 **28.** Fannjiang, A. Raster grid pathology and the cure. *Multiscale Model. & Simul.* **17**, 973–995 (2019).
- 241 **29.** Kim, D. C., Hermerschmidt, A., Dyachenko, P. & Scharf, T. Adjoint method and inverse design for diffractive beam  
242 splitters. In *Components and Packaging for Laser Systems VI*, vol. 11261, 1126115 (International Society for Optics and  
243 Photonics, 2020).
- 244 **30.** Huang, X. *et al.* Optimization of overlap uniformness for ptychography. *Opt. Express* **22**, 12634–12644 (2014).
- 245 **31.** Ackermann, W. a. *et al.* Operation of a free-electron laser from the extreme ultraviolet to the water window. *Nat. photonics*  
246 **1**, 336–342 (2007).

## 247 Acknowledgements

248 The authors would like to thank the entire FLASH team for support during this research. This research was supported in part  
249 through the Maxwell computational resources operated at DESY, Hamburg, Germany. This work was supported through the  
250 DESY young researcher funding with a collaboration initiated within the framework of the PIER graduate school. This project  
251 has received funding from the European Union’s Horizon 2020 Research and Innovation programme under Grant Agreement  
252 No 730872.

253 **Author contributions statement**

254 E.P. and M.M. supervised this work. K.K. and M.M. conceived the idea of experiment and contributed to the development  
255 of the theory and the algorithms. K.K, S.K., M.R-L, B.K. and M.M. designed experiments. J.C, A.M and C.B.W provided  
256 PERCIVAL detector and supported the measurements. All authors performed the experiments as well as contributing to the  
257 data acquisition. K.K. analyzed the data. All authors participated in the writing and the revisions of the manuscript.

258 **Competing interests**

259 The authors declare no competing interests.

260 **Data availability statement**

261 The datasets used and/or analysed during the current study available from the corresponding author on reasonable request.